49th AIAA Aerospace Sciences Meeting including the New Horizons Forum and Aerospace Exposition
4 - 7 January 2011, Orlando, Florida

AIAA 2011-573

Grid and Time Step Requirements to Accurately & Efficiently Resolve Flow around a Rigid Flapping Airfoil using OVERFLOW

Joshua I. Leffell*
Stanford University, Stanford, CA 94305

Thomas H. Pulliam †
NASA Ames Research Center, Moffett Field, CA 94305

Micro air vehicle design is an emerging area in aeronautics requiring accurate solutions of flapping wing flight in combination with numerical optimization. The highly unsteady and complex nature of the flow fields associated with flapping wings can translate to massive computational costs. A large-scale optimization over a significant design space can result in hundreds to thousands of objective evaluations making it critical to ensure maximal efficiency while maintaining the requisite level of accuracy. Full-scale optimization can be used for both the trajectory and geometry of the wings but this work focuses on a reduced two-dimensional problem with fixed geometry. A series of analyses are performed to isolate the minimum spatial and temporal requirements to accurately and efficiently model a two-dimensional flapping rigid airfoil subjected to sinusoidal pitching and plunging motion. NASA's highly parallelized overset flow solver `OVERFLOW` is used for all of the computations on a rigid NACA 0012 airfoil. Grid-spacing and domain size parameters are explored using spatial analysis. The physical time-step with implicit sub-iterations in the context of `OVERFLOW`'s dual time-stepping scheme is explored using temporal analysis. Finally, a method for evaluating periodic convergence in the force and moment time-history signals is discussed.

Nomenclature

f	Flapping frequency, Hz	U_{ref}	Reference velocity
k	Reduced frequency, $\frac{2\pi fc}{U_{ref}}$	Δt	Physical time-step
h	Nondimensional plunge amplitude	N	Number of time-steps per cycle, $\frac{2\pi}{k\Delta t}$
α	Maximum pitch amplitude	N_{SI}	Sub-iterations per Δt
ϕ	Pitch-plunge phase shift	T	Flapping period, $\frac{2\pi}{k}$
a	Pitch axis location	D_x	Length of level-one grid in x-direction
$y(t)$	Vertical position	D_y	Length of level-one grid in y-direction
$\theta(t)$	Rotation angle	Δs	Level one Cartesian grid spacing
c	Chord length	Re	Reynolds number, $\frac{\rho U_{ref} c}{\mu}$
n	Iteration	M_{ref}	Reference Mach number
c_l	Lift coefficient	c_d	Drag coefficient
c_m	Moment coefficient	CCF	Cross-correlation coefficient
$\bar{c}_T$	Time-averaged thrust coefficient	rms	Root mean square
$\bar{c}_P$	Time-averaged power-input coefficient	η_p	Propulsive efficiency, $\frac{\bar{c}_t}{\bar{c}_p}$
f_M	Fuzzy set for time-mean convergence	f_S	Fuzzy set for convergence of signal shape
f_A	Fuzzy set for DFT amplitude convergence	f_ϕ	Fuzzy set for DFT phase convergence

*Graduate Student, Department of Aeronautics & Astronautics and Research Scientist, STC, NASA Ames Research Center, AIAA Student Member. jleffell@stanford.edu
†Senior Researcher, AIAA Associate Fellow. Thomas.H.Pulliam@nasa.gov

I. Introduction

A significant body of research has been performed analyzing periodically forced flows using both experimental and computational methods. Designers of micro air vehicles hope to exploit the highly maneuverable aerodynamics exhibited by birds and insects in their work. A first step in understanding the mechanisms that lead to strong flapping performance is reducing the three-dimensional problem with complex and deformable geometry to a two-dimensional problem using simplified, rigid geometry. A sinusoidally forced airfoil can produce either thrust or drag depending on the frequency and amplitude at which it plunges and pitches. Jones, Dohring and Platzer [1] performed experiments with plunging airfoils and published results of a particular thrust- and lift-producing case. A plunging rigid NACA 0012 airfoil with reduced flapping frequency, $k = 12.3$, and nondimensional plunge amplitude, $h = 0.12$ results in the flow field depicted in Figure 1a. The reference Mach number for this case is $M_{ref} = 0.2$ with Reynolds number, $Re = 1850$. Vorticity computed by an `OVERFLOW` simulation using the same parameters is presented in Figure 1b. Snapshots of vorticity from

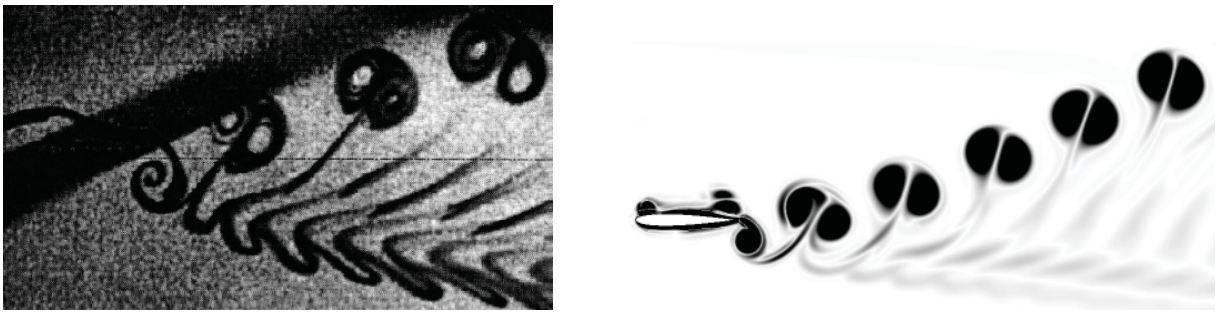

(a) Experimental results from Jones, Dohring & Platzer (b) OVERFLOW solution

Figure 1: Comparison of experimental and computed flow-fields

an `OVERFLOW` simulation at different intervals of the flapping cycle are presented in Figure 2. The paired vortices create thrust by producing a jet of fluid in the downstream direction. Vertical position, y, and the lift and drag signals are plotted in Fig. 3 at intervals corresponding to the labels of Figure 2. At station a the airfoil is moving upwards with a lift deficit. The airfoil has reached the apex of its trajectory by station b with limited lift production. Maximum lift is attained at station c as the airfoil plunges rapidly downwards. Finally, the airfoil reaches the bottom of its stroke with a slight lift deficit at station d. The plunging configuration described and depicted above is used throughout the paper as an example of high-frequency flapping. The reader is directed to references [1-5] for more detailed discussion on the analysis of flapping airfoils.

Modeling flow over flapping geometry can lead to significantly higher computational cost compared to its fixed-body counterpart. Increased resolution in space is required because the body is moving through its domain and may be shedding flow structures such as vortices downstream. Finer temporal resolution is needed to maintain consistency with the unsteady physics of the problem and avoid interpolation errors from excessive grid motion between each time-step. Other costs arise from the need to simulate over a number of flapping cycles until the flow field converges to a periodic state achieving functional invariance of the time-averaged performance measures over the period of a flapping cycle. The ability to isolate the minimum discretization parameters and stop the simulation upon convergence will significantly reduce the computational burden. This computational work is amplified in the context of unsteady optimization where hundreds to thousands of flow solutions are required. The goal of this paper is to understand the spatial and temporal discretization requirements for the reduced two-dimensional problem and establish a reliable method for measuring convergence of the periodic flow to reduce the computational cost of optimization. The spatial investigation includes a grid-spacing study in addition to analysis of solution sensitivity to the domain size. The temporal analysis examines solution dependence on the total number of iterations used per flapping cycle. Finally, a method for analyzing convergence of a periodically forced flow field is introduced and applied. Analyses performed in two-dimensions will hopefully aid future work in three-dimensions where both computational cost and complexity increase significantly.

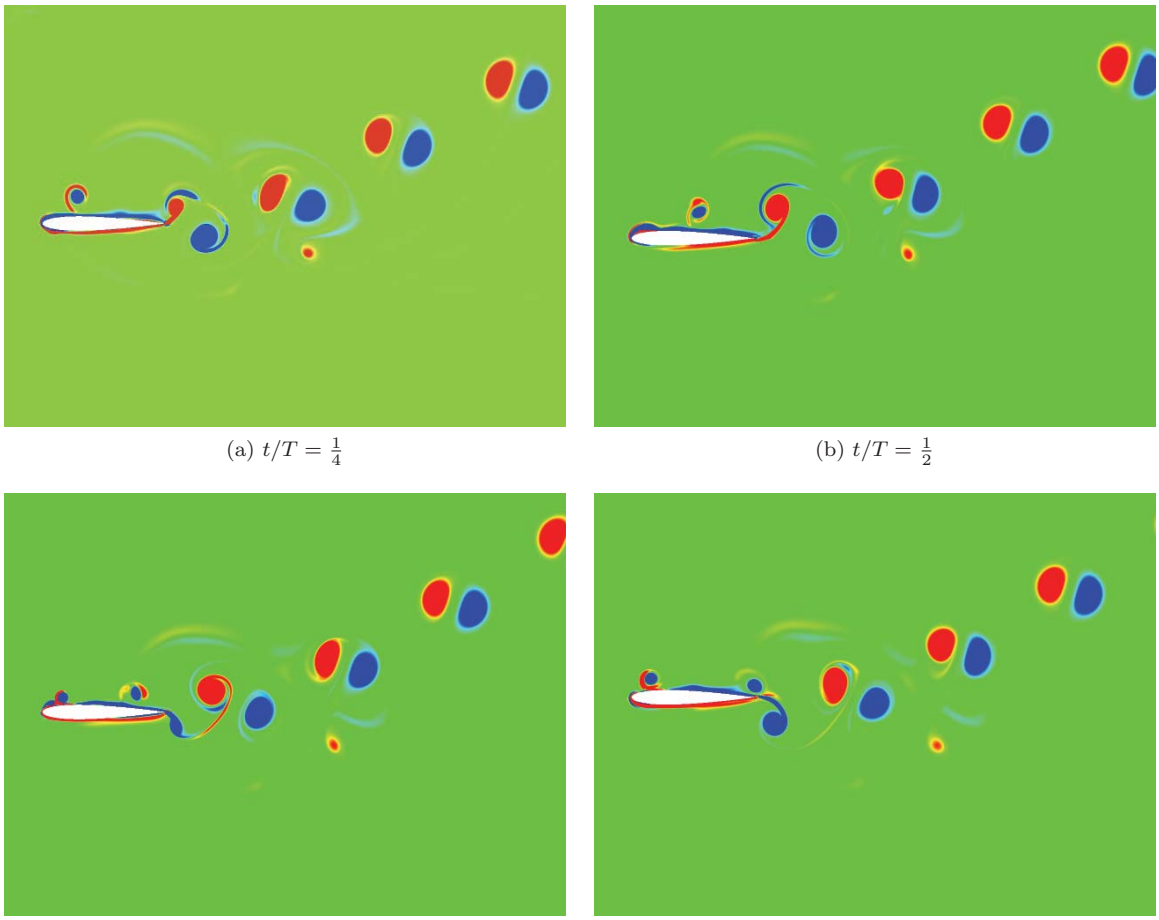

(a) $t/T = \frac{1}{4}$ (b) $t/T = \frac{1}{2}$

(c) $t/T = \frac{3}{4}$ (d) $t/T = 1$

Figure 2: Flow field visualization of vorticity magnitude

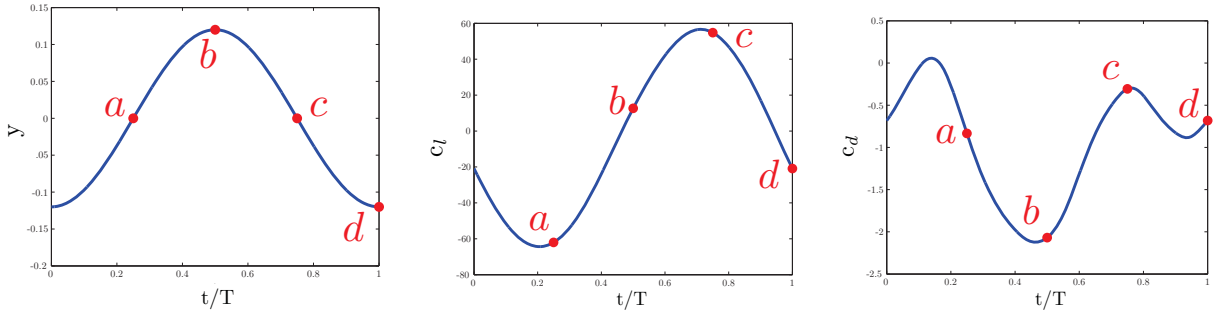

(a) y (b) c_l (c) c_d

Figure 3: y, c_l and c_d at corresponding stations

II. Overflow

OVERFLOW is a highly parallelized overset finite-difference Navier-Stokes flow solver capable of handling grid motion such as flapping airfoils. The code offers several time integration methods and spatial schemes but all simulations presented use second-order implicit dual time-stepping and central differencing in space providing a sixth-order accurate convection operator and a fifth-order accurate dissipation operator. OVERFLOW's overset framework uses a structured body-conforming grid embedded in a set of automatically generated Cartesian off-body grids. X-Rays are used to provide hole-cutting [6] with domain connectivity and interpolation across grid interfaces [7]. A more detailed explanation of the specifics of OVERFLOW can be found in the paper by Nichols, Tramels and Buning [8].

Figure 4 shows an example of a typical two dimensional OVERFLOW grid system (reduced for the purpose of illustration). The curvilinear body-conforming mesh (as seen in orange in Fig. 4a), referred to as the *near-body* grid, is embedded in a series of Cartesian *off-body* grids. The first Cartesian grid is referred to as the *level-one* grid with domain size D_x by D_y with uniform grid-spacing of Δs in both the x- and y-directions (see Fig. 4). The series of Cartesian off-body grids (the second grid is referred to as the *level-two grid* and so on) span the domain to the outer boundaries with each level doubling the previous grid's spacing. Each successive grid level has an overlap region of at least two grid cells of the finer spacing as demonstrated in Fig. 4a between the red and blue hashed lines. The X-Rays corresponding to the near-body grid cut the level-one grid and define an interface through which information will be interpolated between the two grids. Fifth-order spatial discretization requires the use of three fringe, or overlap, points. Figure 4b outlines the X-Ray hole cutting in the upper surface, leading edge region, with a hashed red line.

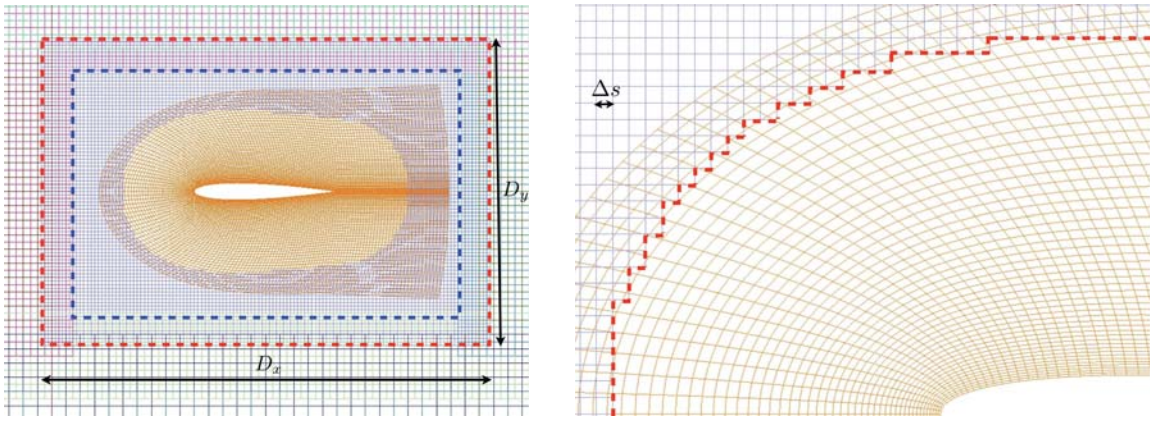

(a) Level-one grid domain (b) X-ray hole cutting

Figure 4: Grid definitions

The solution procedure for a given flapping configuration requires the near-body grids, the X-Rays, surface integration information and an OVERFLOW input file that defines the boundary conditions and essential parameters for the simulation. Two XML files control the grid dynamics. One moves the geometry into its initial position and provides grid-name associativity and the other prescribes the translational and rotational velocities of the associated components. Force and moment coefficients are easily extracted and used to integrate the time-averaged thrust and power-input coefficients as demonstrated in Section IV. Far-field boundaries are placed at 32 chord-lengths in both the positive and negative x- and y-directions for all simulations presented.

III. Kinematics of a Rigid Pitching & Plunging Airfoil

Equations 1 and 2 define the kinematic model of a sinusoidally pitching and plunging rigid airfoil with a frequency of f Hz.

$$y(t) = -h\cos(2\pi f t) \quad (1)$$

$$\theta(t) = -\alpha\cos(2\pi f t + \phi) \quad (2)$$

The airfoil's vertical position, $y(t)$ and the rotation angle, $\theta(t)$, are fully defined by time, t, and five parameters of interest: the reduced frequency, $k = \frac{2\pi f c}{U_{ref}}$, the nondimensional plunge amplitude, h, the maximum pitch amplitude, α, the phase shift between pitching and plunging, ϕ and the pitch-axis along the chord line, a.

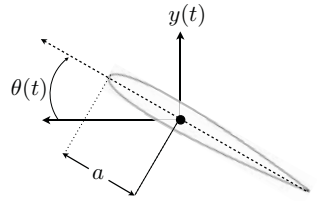

Figure 5: Kinematics of flapping airfoil

These parameters can be used as design variables for optimizing the trajectory of flapping airfoil. A schematic of the kinematics of a rigid flapping airfoil is shown in Figure 5. Full-scale optimization may include the geometry of the flapping body but a NACA 0012 airfoil is used for all of the cases presented.

IV. Analysis of Temporal & Spatial Requirements

Aerodynamic performance can be measured in any number of ways. Force and moment coefficients work well for steady-state problems but flapping wing solutions produce periodic time histories of these functionals without a single value to compare directly with other cases. Computing the time-averaged mean thrust and power-input coefficients, $\bar{c}_T$ and $\bar{c}_P$, provides the analyst with scalar performance measures over a flapping cycle. The ratio of these scalars is defined as the propulsive efficiency of the flapping configuration, η_P. Equations 3-5 define each of these functionals.

$$\bar{c}_T = -\frac{1}{T}\int_t^{t+T} c_d(t)dt \tag{3}$$

$$\bar{c}_P = -\frac{1}{T}\int_t^{t+T} \left(c_l(t)\dot{y}(t) + c_m(t)\dot{\theta}(t)\right) dt \tag{4}$$

$$\eta_P = \bar{c}_T/\bar{c}_P \tag{5}$$

A fitness function to measure flapping performance was constructed by Tuncer and Kaya [9] as a weighted combination of $\bar{c}_T$ and η_P. A generalized objective function, $O(X, S, C)$, is the convex combination of $\bar{c}_T$ and η_P.

$$O\left(X,S,C\right) = \beta\bar{c}_T\left(X,S,C\right) + \left(1-\beta\right)\eta_P\left(X,S,C\right) \text{ where } 0 \leq \beta \leq 1 \tag{6}$$

The independent variables $X = (k, h, \alpha, \phi, a)$ represents the design variables of a given flapping configuration, $S = (\Delta s, D_x, D_y)$ represents the spatial discretization and $C = (\Delta t, N_{SI})$ represents the temporal discretization. Lift, drag and moment coefficients are extracted from the flow solution and $\dot{y}(t)$ and $\dot{\theta}(t)$ are computed analytically by differentiating the expressions for $y(t)$ and $\theta(t)$ in Equations 1 and 2. Further details on optimization of flapping airfoils are provided by Oyama, Okabe, Fujii and Shimoyama [10].

While the objective function is evaluated with the time-averaged integrated functionals of $\bar{c}_T$, $\bar{c}_P$ and η_P, it is critical to examine how the signal shape of the time-history of the integrated force and moment coefficients differ as the spatial and temporal resolutions are adjusted. Two solutions may share a similar thrust coefficient but exhibit significant shape, magnitude and phase differences in the time-history response of the drag coefficient, for example. Two similar signals are guaranteed to have similar time-averaged functionals but similar time-averaged functionals are not guaranteed to have similar signal shape. Clark and Grover [11] define the cross-correlation coefficient, $CCF(f, g)$, which qualifies how well the shape of one signal, f, matches another, g.

$$CCF\left(f,g\right) = \frac{\sum_{n=1}^{N} f\left(n\right)g\left(n\right)}{\left[\sum_{n=1}^{N} f^2\left(n\right)\sum_{n=1}^{N} g^2\left(n\right)\right]^{\frac{1}{2}}} \tag{7}$$

The value of the cross-correlation coefficient ranges from, $0 \leq CCF \leq 1$, where 0 describes no correlation and 1 indicates complete correlation – identical signals. CCF is used to check similarity of a signal from period to period, $g(n) = f(n+N)$, or to check how two individual signals, f and g, compare.

A second measure of signal correlation between two responses compares the root mean square, rms, of each signal over one flapping cycle. This proves a better tool than pure averaging because the force and moment coefficients may vary between positive and negative values over a flapping cycle. Equation 8 defines the root mean square for a signal, f.

$$rms(f) = \sqrt{\frac{1}{N}\sum_{n=1}^{N} f(n)^2} \tag{8}$$

It is important to verify that the analytical tools successfully perform their tasks. Initially, percentage error in thrust coefficient was used to compare signals but this proved inaccurate because certain frequencies' integrated thrust approached zero. Results to be presented later confirm that the quantitative assessments of signal correlation using CCF and rms values agree with qualitative observations.

IV.A. Spatial Requirements

Two spatial discretization factors which greatly influence solutions of flapping airfoil flow are: *a*) the grid spacing near the body and in the region traversed by shed vortices, and *b*) the size of most refined region – the *level-one* grid. A brute-force approach suggests solving on an arbitrarily large domain with exceedingly fine grid spacing. This naturally leads to prohibitive computational costs – especially in the context of optimization that may demand hundreds to thousands of unsteady flow solutions. Grid selection must isolate the minimum spatial requirements to obtain solutions with the requisite level of accuracy. The following two sections explore the sensitivity of flapping airfoil solutions to near-body grid-spacing and level-one domain size over a range of flapping frequencies.

IV.A.1. Grid Spacing

Four near-body grids, with decreasing resolution, are used to determine grid independence for flapping airfoil flow solutions. The goal is to select a near-body grid-spacing that successfully resolves solutions for flapping configurations over a spectrum of flapping frequencies. An optimizer will require solutions to a variety of flapping configurations and it is unreasonable to determine the spatial requirements for each objective function evaluation a priori. The spacing of the level-one grid is chosen to match the spacing of the near-body grid in the overlap region to ensure high-quality interpolation between the two grids. Table 1 provides information about each of the grids where index j runs tangential to the airfoil and index k runs normal to the airfoil in a structured c-mesh. The first point normal to the airfoil in k is $0.0036c$ for each grid.

Grid #	n_j	n_k	$n_{Airfoil}$	L1 Pts	Δs
1	1601	201	1025	6,352,020	$0.0025c$
2	801	151	513	1,603,305	$0.005c$
3	401	101	257	407,721	$0.01c$
4	201	51	129	71,145	$0.025c$

Table 1: Near-body grid points in j, in k, along the airfoil, level-one (L1) grid-points and grid-spacing

The objective functional for pure plunging is computed based on the lift and drag coefficients. Of these, the drag coefficient is the slowest to converge and as such it will be used to determine grid independence. Figure 6 shows the c_d signal of the 24th (re: converged) flapping cycle for the four test case frequencies. The highest frequency cases use the configuration outlined in Section I. The frequency of $k = 12.3$ is halved three times arriving at the four test frequencies: $k = 1.5375$, 3.075, 6.15 and 12.3. All cases are pure plunging with $h = 0.12$. The level-one grid domain size is $D_x \times D_y = 13c \times 3c$ with the airfoil placed such that $\frac{3}{4}$ of the level-one domain remains downstream. Each case uses 2000 time-steps per cycle (N) and 10 implicit sub-iterations (N_{SI}) as defined in Section IV.B.

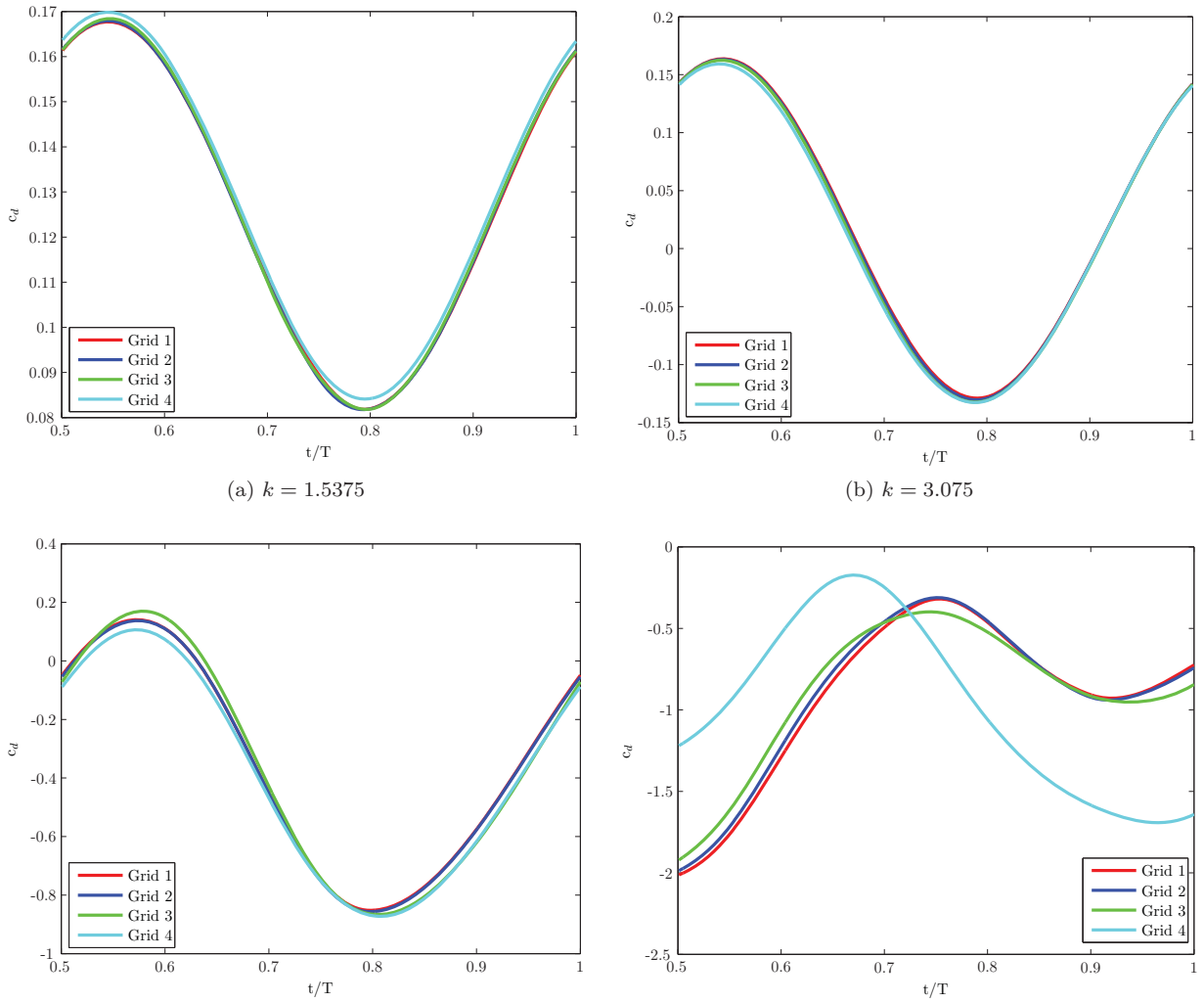

(a) $k = 1.5375$ (b) $k = 3.075$

(c) $k = 6.15$ (d) $k = 12.3$

Figure 6: c_d signal for different flapping frequencies, k, over half a flapping period, T

The cross-correlation coefficient and percent error in root mean square of the drag signal between grids 2-4 and the finest grid (Grid 1) are presented in Table 2. Error in rms, e_{rms}, provides more meaningful results than error in thrust coefficient because $\bar{c}_T$ is an integral of positive and negative values. If the integration results in a small number (as is the case for the for the $k = 3.075$ configuration) then the quantitative error calculation can differ greatly from the observed qualitative error. Equation 9 defines percent error in rms for a signal f.

$$\%e_{rms} = 100 \times \left| \frac{rms\,(f) - rms\,(f_{exact})}{rms\,(f_{exact})} \right| \tag{9}$$

In Table 2, CCF and e_{rms} are computed for each grid taking the c_d signal of the finest grid as exact.

	Grid 2		Grid 3		Grid 4	
k	CCF	e_{rms}	CCF	e_{rms}	CCF	e_{rms}
1.5375	0.9999	0.171%	0.9999	0.407%	0.9999	1.75%
3.075	0.9999	0.0834%	0.9995	0.472%	0.9986	0.720%
6.15	0.9999	0.427%	0.9985	2.81%	0.9986	3.74%
12.3	0.9999	0.280%	0.9973	3.13%	0.8284	7.60%

Table 2: c_d signal comparison for each test frequency

The signal quality of c_d is satisfactory for the three coarser grids at the lower frequencies of $k = 1.5375$, 3.075 and 6.15. However, the correlation of c_d signal for $k = 12.3$ on the coarsest grid (Grid 4) is unacceptable because of substantial magnitude and phase errors. The error estimates agree with observed results in Fig. 6d where $CCF = 0.8284$ and $e_{rms} = 7.60\%$. Grid 3 sufficiently resolves the drag signal for each test frequency and will thus be used for much of the remaining analysis to save considerable computational cost over the two finer grids.

IV.A.2. Domain Size

A second task in grid selection is determining an appropriate level-one domain size. The solution at every grid point in the entirely subsonic domain influences the solution at every other point. Thus, the solution at every point in the domain contributes to the force and moment functional values. The significance of the contribution, however, is unknown but it is clear that points *near* the boundary are important warranting an investigation into the solution sensitivity of level-one grid size.

Label	C1	C2	C3	C4	U1	U2	U3	U4	Control
D_x	$5c$	$9c$	$17c$	$33c$	$5c$	$9c$	$17c$	$33c$	$33c$
D_y	$4c$	$4c$	$4c$	$4c$	$4c$	$4c$	$4c$	$4c$	$16c$
Points	$\approx 200k$	$\approx 360k$	$\approx 680k$	$\approx 1320k$	$\approx 200k$	$\approx 360k$	$\approx 680k$	$\approx 1320k$	$\approx 5280k$

Table 3: Level-one domain size information

Two flapping configurations are solved on a series of level one domains to investigate the solution sensitivity to domain size and the location of the airfoil within that domain. A low-frequency case of combined pitching and plunging and a high-frequency case of pure plunging are included to derive insight into the domain requirements throughout a reasonable design space of flapping parameters, X. Additionally, the location of the airfoil within the domain is included in the analysis. In the cases examined, large vortical structures produced by the flapping motion are convected downstream of the airfoil. This suggests placing the airfoil upstream of the domain's center to resolve more of these structures on a finer mesh for a longer period of time. The sizes of the level-one domain used are defined in Table 3. Grid labels beginning with a C- prefix indicate central placement of the airfoil whereas a U- prefix refers to upstream airfoil placement. A control domain is used to compute the CCF and e_{rms}. It extends 33 chord-lengths in x and 16 chord-lengths in y with the airfoil in the center resulting in a level-one grid with approximately 5.3 million grid-points. For upstreamed-centered cases, the airfoil is placed such that $\frac{3}{4}$ of the level-one domain remains downstream. Grid 3 from the previous section is used as the near-body grid with $\Delta s = 0.01$, $N = 2000$ physical time-steps per cycle and $N_{SI} = 10$ implicit sub-iterations per time-step. Signals are extracted from the 10th flapping period.

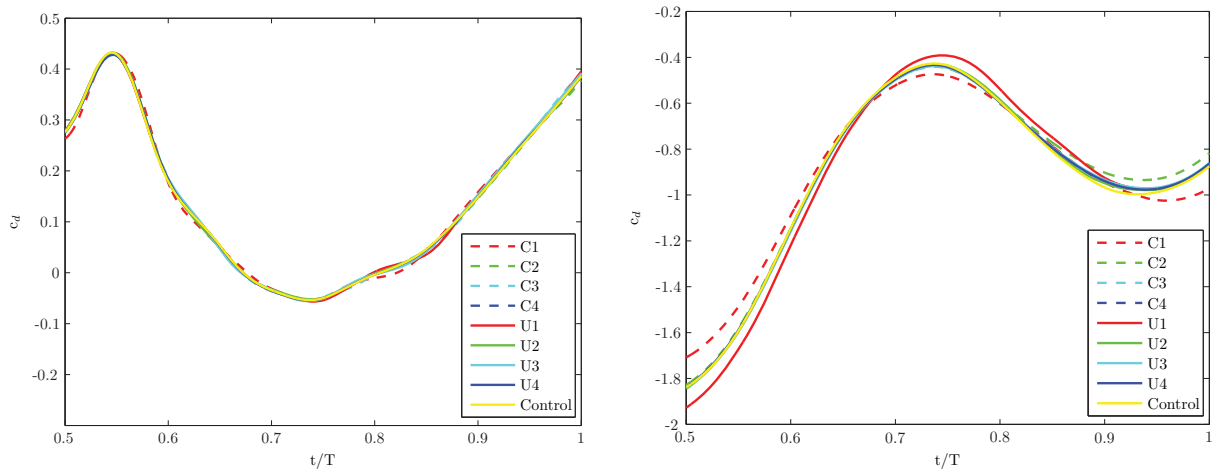

(a) Low-frequency pitching & plunging
$k = 1$, $h = 0.5$, $\alpha = 5°$, $\phi = 30°$

(b) High-frequency plunging
$k = 12.3$, $h = 0.12$, $\alpha = 0°$, $\phi = 0°$

Figure 7: c_d dependence on *level-one* grid domain size and airfoil location

Figure 7 demonstrates the increased sensitivity to level-one domain size for the high-frequency case. The smallest domain ($D_x = 5c$) was sufficient for resolving the low frequency case but not the high frequency plunging case. Tables 4 and 5 quantitatively demonstrate the increased domain size dependence for the high frequency case. CCF and rms values compare each grid to the control.

	Center		Upstream	
$D_x \times D_y$	CCF	e_{rms}	CCF	e_{rms}
$5c \times 4c$	0.9996	0.0905%	0.9998	0.172%
$9c \times 4c$	0.9998	0.441%	0.9999	0.365%
$17c \times 4c$	0.9998	0.0111%	0.9999	0.324%
$33c \times 4c$	0.9999	0.0455%	0.9999	0.125%

Table 4: Signal comparison for $k = 1$, $h = 0.5$, $\alpha = 5°$, $\phi = 30°$

	Center		Upstream	
$D_x \times D_y$	CCF	e_{rms}	CCF	e_{rms}
$5c \times 4c$	0.9989	3.78%	0.9986	1.66%
$9c \times 4c$	0.9998	1.56%	0.9999	0.561%
$17c \times 4c$	0.9999	0.586%	0.9999	0.647%
$33c \times 4c$	0.9999	0.598%	0.9999	0.594%

Table 5: Signal comparison for $k = 12.3$, $h = 0.12$, $\alpha = 0°$, $\phi = 0°$

The smallest domain, with the airfoil centered or located upstream, is satisfactory for the lower-frequency case while the high-frequency case demands a domain that spans at least 9 chord lengths in the x-direction. Placing the airfoil upstream improves the solution for the smallest and second to smallest domains as it allows for finer resolution of vortices in the proximity of the airfoil. There is still much to be explored in establishing grid requirements for forced periodic flows but proximity- and feature-based adaption will assist in automating the process by dynamically generating new grids to resolve desired features such as vortices convecting throughout the domain.

IV.B. Temporal Requirements

OVERFLOW's use of implicit dual time-stepping requires selection of a physical time-step, Δt, and the number of implicit sub-iterations, N_{SI}, to be performed at each time-step. The combination of Δt and N_{SI} must sufficiently model the physics of the problem while reducing the residual at each time-step by a reasonable amount to ensure a commensurate level of accuracy. There are additional temporal parameters built into the code such as maximum CFL and local time-step but discussion here is limited to Δt and N_{SI}. OVERFLOW's implicit dual time-stepping scheme, described in Eq. 10, uses both physical time, t, and computational time, τ, to iterate the solution forward.

$$\frac{dQ}{d\tau} + \frac{dQ}{dt} + F\left(Q\left(t\right)\right) = 0 \tag{10}$$

where Q is a vector of the flow-variables and F represents the inviscid and viscous flux terms of the Navier-Stokes equations. Applying second-order implicit differencing in t and first-order implicit differencing in τ,

$$\frac{Q^{s+1} - Q^s}{\Delta\tau} + \left[\frac{3Q^{s+1} - 4Q^n + Q^{n-1}}{2\Delta t} + F\left(Q^{s+1}\right)\right] = 0 \tag{11}$$

Linearizing in s results in Eq. 12 where $L\left(Q^s\right)$ is the implicit linear driver with sub-iterations advancing in s, i.e. $s = 1, \ldots, N_{SI}$.

$$L\left(Q^s\right)\left(Q^{s+1} - Q^s\right) = -\left[\frac{3Q^s - 4Q^n + Q^{n-1}}{2\Delta t} + F\left(Q^n\right)\right] = -R\left(Q^s, Q^n\right) \tag{12}$$

$R\left(Q^s, Q^n\right)$ in Eq. 12 is the residual at time-step n and sub-iteration s. The norm of R, $||R||$, measures sub-iteration convergence. In the context of optimization, temporal resolution must be selected such that computational resources are not wasted by solving more time-steps per flapping cycle than necessary or driving the residual beyond a necessary level with superfluous implicit sub-iterations. A parametric study is performed to determine appropriate values for Δt and N_{SI}. The low- and high-frequency flapping configurations from the domain size study in Sec. IV.A.2 are used. For consistency among the different frequencies Δt is defined as:

$$\Delta t = \frac{2\pi}{kN} \tag{13}$$

Results using a range of N and N_{SI} values are computed to demonstrate solution trends as the number of total iterations per flapping cycle, $N \times N_{SI}$, increases to a maximum value of 128,000. Figures 8 and 9 show the root mean square of the drag signals for the low- and high-frequency cases, respectively. The root mean square of the drag coefficient is plotted as a function of total iterations per cycle. Figures 8a and 9a plot the root mean square of drag as a function of total iterations per flapping cycle for different values of N where N_{SI} increases for each data-point moving from left to right. Figures 8b and 9b plot the root mean square of drag as a function of total iterations per flapping cycle for different values of N_{SI} where N increases for each data-point moving from left to right. Signals are extracted from the 10th flapping period.

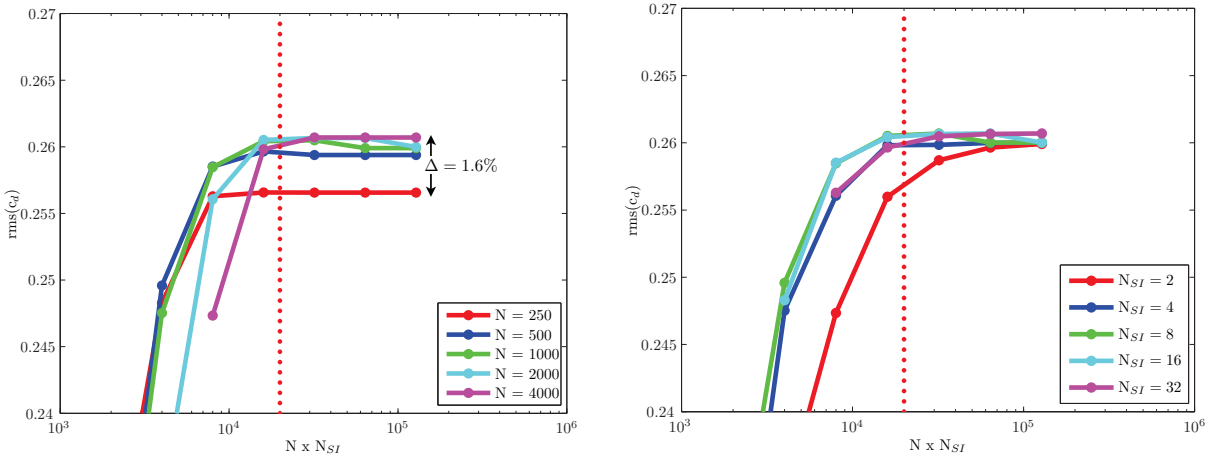

(a) N vs $N \times N_{SI}$ (b) N_{SI} vs $N \times N_{SI}$

Figure 8: $rms(c_d)$ for $k = 1$, $h = 0.5$, $\alpha = 5°$, $\phi = 30°$

Figures 8a and 8b show that using most values of N and N_{SI} will converge as the total number of iterations per cycle increases. Figure 8a shows that combinations of total iterations per cycle using $N = 250$ fail to completely converge in the limit of $N \times N_{SI}$. The percentage error in rms for $N = 250$ versus $N = 4000$ for the maximum number of total iterations is 1.6%. Comparatively, the error in rms for $N_{SI} = 2$ versus $N_{SI} = 32$ is only 0.298% for the maximum number of total iterations. These plots show that once a certain number of iterations is reached, $N \times N_{SI} \approx 2 \times 10^4$ (see dotted red lines), the specific values of N and N_{SI} are free to change contingent upon $N \geq 500$. Using $N = 250$ results in a physical time-step that may be too large to capture all of the unsteady physics of the flow.

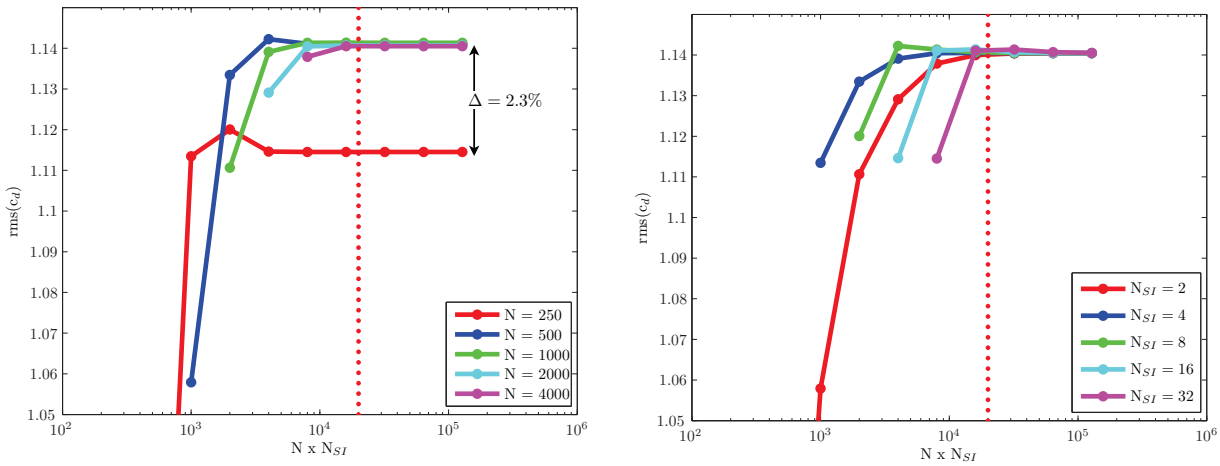

(a) N vs $N \times N_{SI}$ (b) N_{SI} vs $N \times N_{SI}$

Figure 9: $rms(c_d)$ for $k = 12.3$, $h = 0.12$, $\alpha = 0°$, $\phi = 0°$

Results for the high-frequency case presented in Fig. 9 offers similar temporal guidelines for the low-frequency case. Figures 9a and 9b show that solutions using $N = 250$ will not converge to a consistent value in the limit of total iterations per cycle. It appears that this flapping configuration also requires approximately 2×10^4 total iterations for all solutions to fully converge. The error in rms for $N = 250$ for the maximum of total iterations per cycle is 2.3% whereas the error in rms for N_{SI} for the maximum number of total iterations is only 0.0056%. Again, a simulation using too large a physical time-step will never converge in the limit of temporal resolution. Using a small number of implicit sub-iterations with a large number of time-steps per cycle will converge for both flapping configurations at which point the scheme essentially reverts back to a single time-stepping method. These examples only demonstrate convergence in

the limit of temporal resolution and do not address overall accuracy of the solution.

While determination of a threshold for iterations required per cycle can serve as a guideline it should not be followed dogmatically as temporal convergence can be achieved with significantly less resolution.

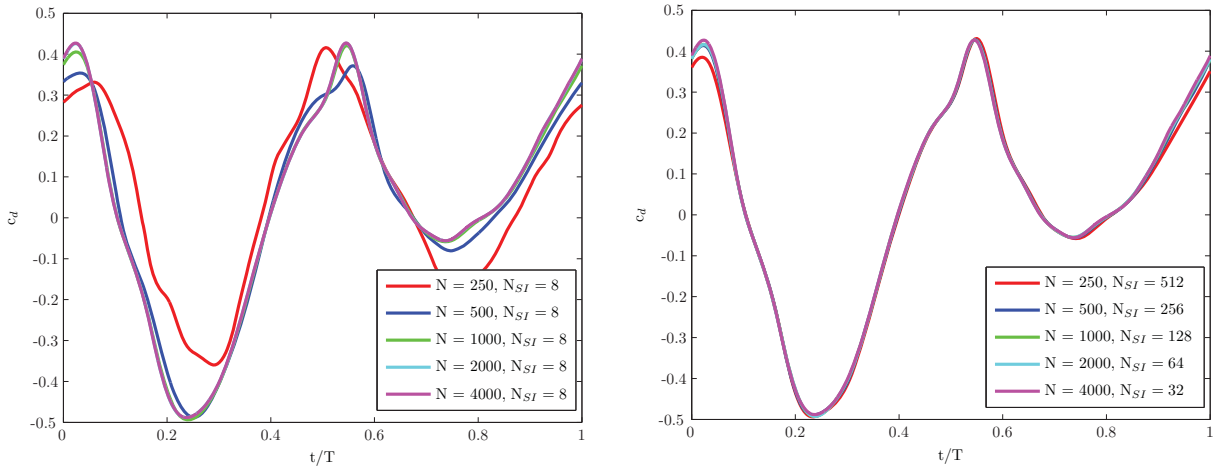

(a) c_d for constant $N_{SI} = 8$ (b) c_d for maximum $N \times N_{SI} = 128,000$

Figure 10: Comparison of c_d signal between $N_{SI} = 8$ and maximum iterations for $k = 1$, $h = 0.5$, $\alpha = 5°$, $\phi = 30°$

Figure 10 shows that the drag signal for the low-frequency case fails to converge to if fewer than 1000 time-steps per cycle are combined with only 8 sub-iterations but that all combinations converge in the limit of temporal resolution with limited exception to the $N = 250$ case. Thus, at least 8000 total iterations per flapping cycle are required to resolve the low-frequency case. Figure 11b shows that the drag signals for all but $N = 250$ converge in the limit of iterations per flapping cycle for the high-frequency case but Fig. 11a shows that convergence in the drag signal is achieved for $N = 500$ with only eight sub-iterations totaling only 4000 iterations per flapping cycle and less than the low-frequency case. Pitching and increased plunging amplitude in the low-frequency case necessitates increased temporal resolution.

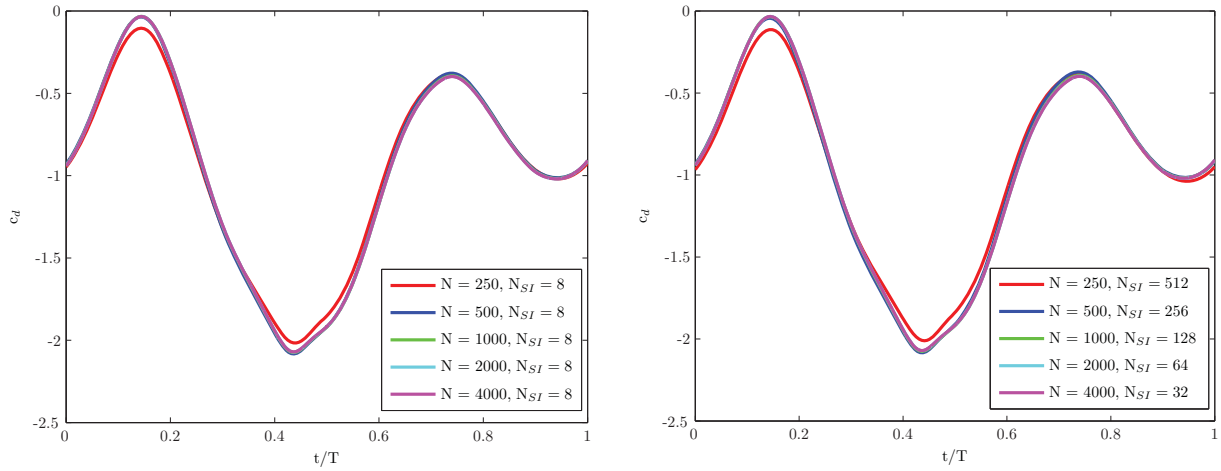

(a) c_d for constant $N_{SI} = 8$ (b) c_d for maximum $N \times N_{SI} = 128,000$

Figure 11: Comparison of c_d signal between $N_{SI} = 8$ and maximum iterations for $k = 12.3$, $h = 0.12$

The total iterations per cycle required for these cases are significantly less than the threshold discussed above and a small fraction of the maximum iterations used. The threshold can be used as an initial estimate but less iterations have proven to be sufficient for both test cases.

It would be beneficial to monitor the solution during the computation to determine if adjusting temporal parameters could reduce the wall-time necessary to reach a periodic unsteady convergence. One way to achieve this would be reducing the number of time-steps per cycle or implicit sub-iterations. Another approach would increase the number of time-steps per cycle with the goal of reducing the number of flapping cycles for the solution to enter a periodic state.

V. Periodic Unsteady Convergence

Solutions of flapping airfoils require the computation of multiple flapping cycles before the flow field reaches a periodic state. The work required to reach this periodic state is dependent upon the kinematic parameters of the flapping configuration in addition to spatial and temporal discretization. Because the flow is periodically forced by flapping the airfoil, the force and moment functionals will converge to a periodic signal as opposed to fixed values. Clark and Grover [11] refer to this type of convergence as *periodic unsteady convergence*. Terminating the computation upon first reaching unsteady periodic convergence can provide significant computational savings especially in the context of optimization.

The objective function, defined in Eq. 6, is a convex combination of the time-averaged thrust and propulsive efficiency coefficients. Monitoring convergence of these two functionals, or the objective function directly, is straightforward. As previously mentioned, similar values of the thrust and power coefficients can be generated from dissimilar force and moment time-history signals. A more robust method of convergence estimation must be employed to evaluate the correlation of functional signal shape from one cycle to the next to guarantee a periodically converged flow field.

Clark and Grover [11] present one such framework for assessing periodic unsteady convergence. A methodology is developed for computing a global measure of periodic unsteady convergence by creating a series of fuzzy sets that each describe membership into unique elements of periodic unsteady convergence. Clark and Grover [11] use pressure signals from an array of sample-points in the domain to monitor time-averaged fluctuations, Discrete Fourier Transform (DFT) magnitudes and phases, cross-correlation coefficients and power spectral densities at each flapping cycle. Values from the current and previous cycle are compared to determine the degree of convergence in each measure after every flapping period. Clark and Grover [11] employ multi-valued logic to produce an additional fuzzy set represented by a single value, f_c, describing overall convergence of the unsteady periodic solution. Fuzzy sets for mean-level, amplitude, phase angle and overall signal shape are employed. Integrated pressure on the surface of the airfoil provides time-history signals for the force and moment coefficients. Because the force and moment time-history signals vary between positive and negative values, the root-mean-square is used in the time-mean fuzzy sets instead of pure averaging. CCF and rms are defined previously in Eqs. 7 and 8, respectively. Equations 14-15 define the magnitude, A, and phase, ϕ, for a DFT represented by P.

$$A = 2\frac{|P|}{N} \tag{14}$$

$$\phi = \tan^{-1}\left(\frac{\Im(P)}{\Re(P)}\right) \tag{15}$$

Membership grade in a fuzzy set varies between 0 and 1, $0 \leq f \leq 1$, where 0 suggests no membership in the fuzzy set f and 1 indicates complete membership. Unlike boolean logic, partial membership in fuzzy sets is permitted. More information on the theory and application of fuzzy sets can be found in Klir and Yuan [12]. Equations 16-19 define the fuzzy sets for mean-value, DFT amplitude, DFT phase and signal shape, respectively.

$$f_M = 1 - \left|1 - \frac{rms(c_2)}{rms(c_1)}\right| \tag{16}$$

$$f_A = 1 - \left|1 - \frac{A_2}{A_1}\right| \tag{17}$$

$$f_\phi = 1 - \left|\frac{\phi_2 - \phi_1}{\pi}\right| \tag{18}$$

$$f_S = CCF(c_1, c_2) \tag{19}$$

The subscripts of 2 and 1 in the fuzzy set definitions in Eqs. 16-19 indicate the current and previous flapping cycle, respectively. The c refers to a force or moment coefficient signal. In practice, three fuzzy sets, f_{M,c_l},

f_{M,c_d} and f_{M,c_m}, are defined to monitor the root-mean-square convergence for the lift, drag and pitching moment coefficients at each cycle. Three additional fuzzy sets, f_{S,c_l}, f_{S,c_d} and f_{S,c_m}, are constructed to monitor the signal shape of the three force and moment coefficients using the cross-correlation coefficient. The spectral-based fuzzy sets of f_A and f_ϕ are computed for the fundamental frequency of each force and moment coefficient. In summary, there are a total of three instances (corresponding to c_l, c_d and c_m) of each of the four fuzzy set categories, f_M, f_A, f_ϕ and f_S.

The values of Eqs. 16-19 define the degree of membership in each fuzzy set. Global convergence, f_c, is treated as a fuzzy set characterized by the intersection of the other sets.

$$f_c = f_M \cap f_A \cap f_\phi \cap f_S \tag{20}$$

The intersection of fuzzy sets are defined as

$$f_c = \min\left(f_M, f_A, f_\phi, f_S\right) \tag{21}$$

Thus, overall convergence is evaluated as the weakest membership grade in any sub-global set after each cycle. Clark and Grover [11] suggest that two consecutive cycles with $f_c \geq 0.95$ implies convergence of the periodic unsteady flow field.

A time-history of the membership grade for each of the 12 non-global fuzzy sets for the high-frequency case is presented in Figure 12a. The coarsest grid, Grid 4, from Sec. IV.A.1 was used with $N = 2000$ and $N_{SI} = 10$. Fuzzy-sets corresponding to the drag signal are the slowest to reach the tolerance level of 0.95 designated by the dotted black line. The corresponding drag coefficient time-history is plotted in Fig. 12b for comparison.

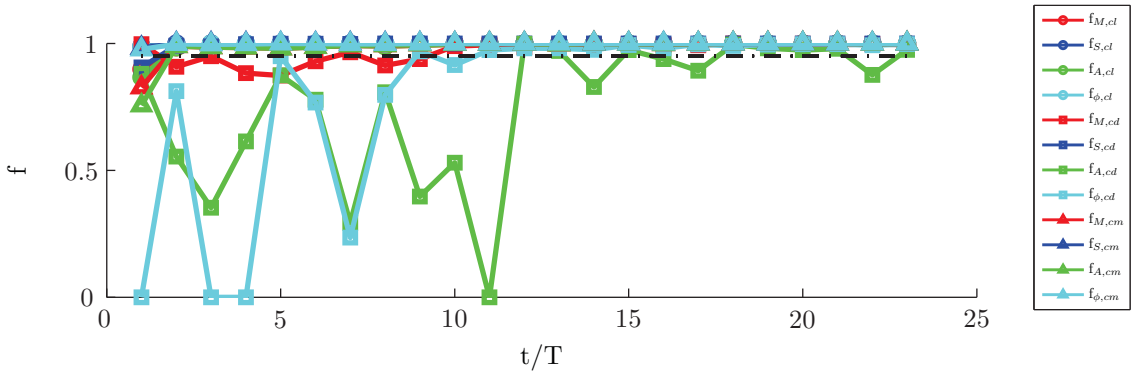

(a) Non-global fuzzy sets

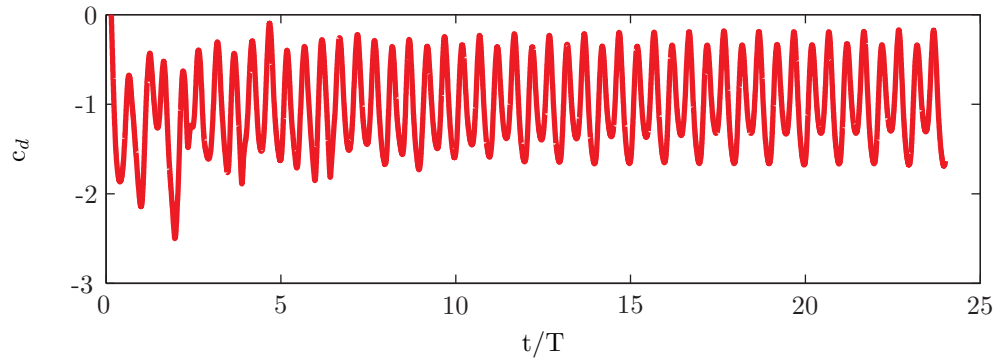

(b) c_d

Figure 12: Time history of drag coefficient, c_d, and non-global fuzzy sets for $k = 12.3$, $h = 0.12$

Each of the four test-cases described in Sec. IV.A.1 are analyzed for periodic unsteady convergence over a range of time-steps per cycle: $N = (250, 500, 1000, 2000, 4000)$. Ten implicit sub-iterations, N_{SI}, are used

in each case. The three lower-frequency configurations converge rapidly but the high-frequency configuration requires significantly more cycles to converge. The iterations required for each of the test-cases to converge is provided in Table 6. The time-histories of the thrust coefficients and global fuzzy sets, f_c, using $N = 2000$ are presented in Figures 13-16 to demonstrate typical evolution of the drag signal for each case.

k	N	Grid 1	Grid 2	Grid 3	Grid 4
1.5375	250	3	3	3	3
	500	3	3	3	3
	1000	3	3	3	3
	2000	3	3	3	3
	4000	3	3	3	3
3.075	250	3	3	3	3
	500	3	3	3	3
	1000	3	3	3	3
	2000	3	3	3	3
	4000	3	3	3	3
6.15	250	3	3	3	3
	500	3	3	3	3
	1000	3	3	3	3
	2000	3	3	3	3
	4000	3	3	3	3
12.3	250	8	8	8	19
	500	8	9	7	11
	1000	8	11	8	13
	2000	8	11	8	13
	4000	8	11	8	13

Table 6: Number of flapping cycles computed before reaching periodic unsteady convergence for each grid at each frequency and for each number of time-steps per cycle

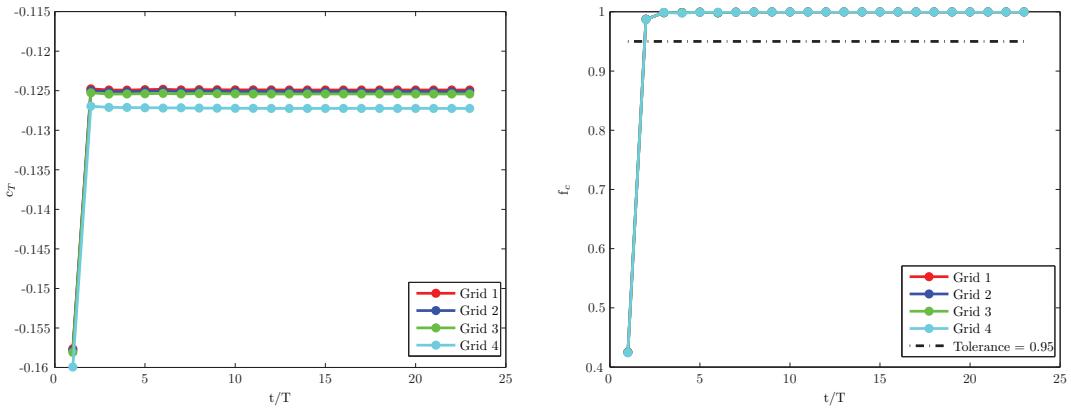

(a) $\bar{c}_T$ (b) f_c

Figure 13: Time history of thrust coefficient, $\bar{c}_T$, and global fuzzy set, f_c for $k = 1.5375$, $h = 0.12$

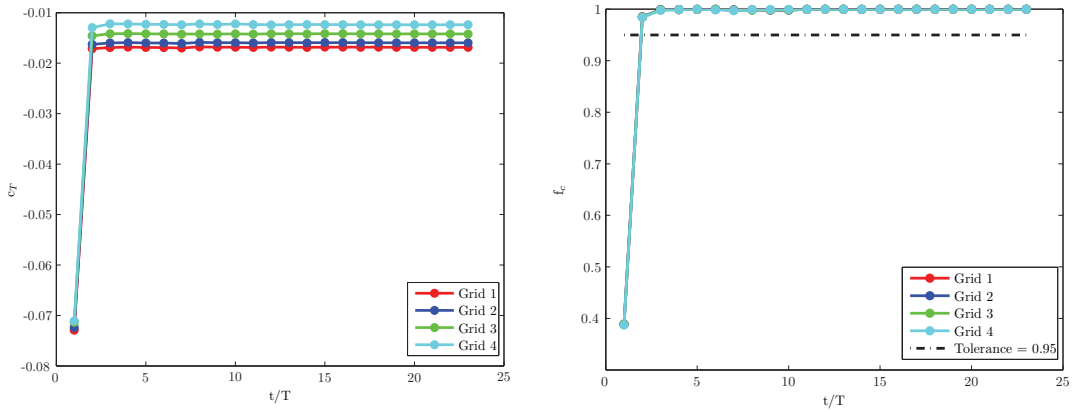

(a) $\bar{c}_T$ (b) f_c

Figure 14: Time history of thrust coefficient, $\bar{c}_T$, and global fuzzy set, f_c $k = 3.075$, $h = 0.12$

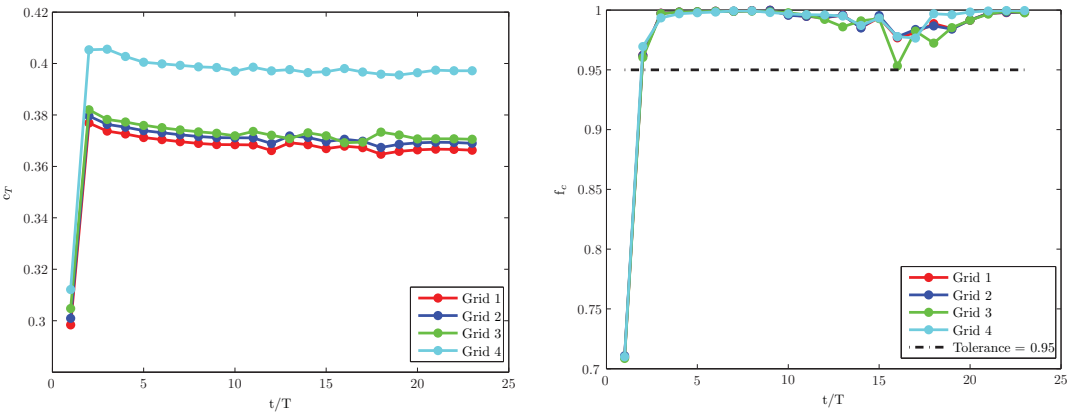

(a) $\bar{c}_T$ (b) f_c

Figure 15: Time history of thrust coefficient, $\bar{c}_T$, and global fuzzy set, f_c for $k = 6.15$, $h = 0.12$

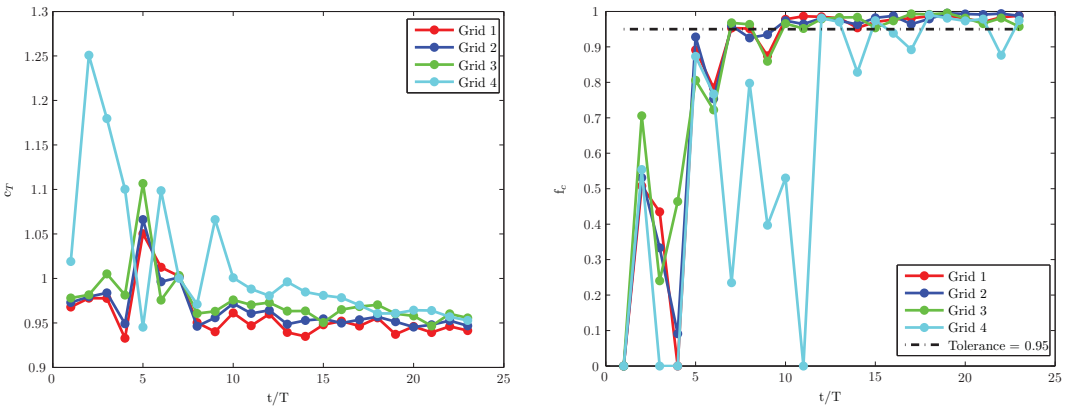

(a) $\bar{c}_T$ (b) f_c

Figure 16: Time history of thrust coefficient, $\bar{c}_T$, and global fuzzy set, f_c for $k = 12.3$, $h = 0.12$

The lower-frequency cases shown in Figures 13-15 converge rapidly for all values of N and on each level of grid resolution while f_c for the higher frequency case fluctuates for each grid resolution. The spectral

fuzzy sets, f_A and f_ϕ, for drag are the most resistant to convergence in this case.

Periodic unsteady convergence analysis provides key insights into the behavior of solutions with different flapping parameters and spatial and temporal discretizations but it does not account for accuracy. Accuracy is controlled by the spatial and temporal discretization discussed in the previous section, whereas, convergence is primarily controlled by the flapping configuration. This is exemplified by the slow convergence for the high-frequency case for all temporal and spatial discretizations. The overall goal is to balance convergence rate with sufficient accuracy.

VI. Summary

This work focused on understanding how spatial and temporal discretization affect solutions to flapping airfoil simulations over a range of flapping parameters in the context of `OVERFLOW`'s overset grid and dual time-stepping frameworks. Informative signal processing error estimators were introduced and verified. Two types of spatial analysis were performed that focused on grid-spacing in near-body grid and domain size of the level-one gird. Temporal analysis investigated the interplay between time-steps per cycle and implicit sub-iterations per time-step and suggests that solutions converge in the limit of iterations per cycle for all but the largest physical time-steps. Insight gained studying the two-dimensional process will be applied to three-dimensional cases where selection of controlling parameters becomes less obvious. This was by no means an exhaustive study but key trends in solution sensitivity to spatial and temporal discretizations were uncovered.

A method to measure periodic convergence was applied based on the work of Clark and Grover [11]. This demonstrated that convergence rate is highly dependent on the flapping configuration. Future plans include development of a monitoring process to analyze solution convergence during the simulation. An additional process aimed at controlling the convergence of a simulation by dynamically adjusting the quantity of sub-iterations or the time-step size will also be addressed. All of these efforts are directed at the development of an efficient framework for optimization of forced periodic flows.

Acknowledgments

This work is funded by the Army High Performance Computing Research Center (AHPCRC). The authors would like to thank NASA Advanced Supercomputing for use of their facilities.

References

[1]Jones, K.D., Dohring, C. M., and Platzer, M. F. 1998. "Experimental and Computational Investigation of the Knoller-Betz Effect," *AIAA Journal*, 36(7): 1240-1246

[2]Young, J. and Lai, J. C. S. 2007. "Vortex Lock-In Phenomenon in the Wake of a Plunging Airfoil," *AIAA Journal*, 45(2): 485-490

[3]Lai, J. C. S., and Platzer, M. F. 1999. "Jet Characteristics of a Plunging Airfoil," *AIAA Journal*, 37(12):1529-1537

[4]Platzer, M.F, and Jones, K.D. 2006. "Flapping Wing Aerodynamics - Progress and Challenges," *44th AIAA Aerospace Sciences Meeting and Exhibit*, Reno, NV, paper no. AIAA-2006-500

[5]Ashraf, M. A., Young, J., and Lai, J. C. S. 2009. "Effect of Airfoil Thickness, Camber and Reynolds Number on Plunging Airfoil Propulsion," *47th AIAA Aerospace Sciences Meeting Including The New Horizons Forum and Aerospace Exposition*, Orlando, FL, paper no. AIAA-2009-1274

[6]Chan, W. M. 2009. "Overset Grid Technology Development at NASA Ames Research Center," *Computers and Fluids*, 38(3): 496-503.

[7]Meakin, R. L. 2001. "Automatic Off-body Grid Generation for Domains of Arbitrary Size," *AIAA 15th Computational Fluid Dynamics Conference*, Anaheim, CA, paper no. AIAA-2001-2536.

[8]Nichols, R. H., Tramel, R. W., and Buning, P. G. 2006. "Solver and Turbulence Model Upgrades to OVERFLOW 2 for Unsteady and High-speed Applications," *24th AIAA Applied Aerodynamics Conference*, San Francisco, CA, paper no. AIAA-2006-2824.

[9]Tuncer, I. H., and Kaya, M. 2005. "Optimization of Flapping Airfoils for Maximum Thrust and Propulsive Efficiency," *AIAA Journal*, 43(11): 2329-2336

[10]Oyama, A., Okabe, Y., Fujii, K., and Shimoyama, K. 2007. "A Study on Flapping Motion for MAV Design Using Design Exploration," *AIAA 2007 Aerospace Sciences Conference*, Rohnert Park, CA, paper no. AIAA-2007-2878.

[11]Clark, J.P., and Grover, E.A. 2006. "Assessing Convergence in Predictions of Periodic-Unsteady Flowfields," *ASME TURBO EXPO 2006: Power for Land, Sea and Air*, Barcelona, Spain, 1-11

[12]Klir, G. J. and Yuan, B., 1995. "Fuzzy Sets and Fuzzy Logic: Theory and Applications," *Prentice Hall PTR*, Upper Saddle River, NJ.